

FINITE-ELEMENT SIMULATION OF INCOMPRESSIBLE VISCOUS FLOWS IN MOVING MESHES

Tony W. H. Sheu^{1,2,3} and M. C. Hsu¹

¹Department of Engineering Science and Ocean Engineering, National Taiwan University, Taipei, Taiwan, Republic of China

²Taida Institute of Mathematical Science (TIMS), National Taiwan University, Taipei, Taiwan, Republic of China

³Center for Quantum Science and Engineering (CQSE), National Taiwan University, Taipei, Taiwan, Republic of China

This study aims to develop a two-dimensional dispersion relation-preserving Petrov-Galerkin finite-element model for effectively resolving convective instability in the simulation of incompressible viscous fluid flows in moving meshes. The developed test functions, which accommodate better dispersive nature, are justified through the convection-diffusion equation and the Navier-Stokes equations. For moving-boundary problems, the fluid flows over an oscillating square cylinder and are investigated in the contraction-and-expansion channel. Through several benchmark tests, the dispersion relation-preserving Petrov-Galerkin finite-element model developed within the arbitrary Lagrangian-Eulerian formulation has been shown to be highly reliable to investigate a wide range of incompressible flow problems in moving meshes.

1. INTRODUCTION

The subject of resolving the computational difficulty related to the inherent divergence-free velocity vector in incompressible Navier-Stokes equations, cast in their primitive-variables form, has been a challenging simulation task for many decades. Suppressing the predicted velocity oscillations due to the erroneous treatment of advection terms has been known to be another major difficulty. Besides the stability consideration, the prediction quality should also be judged from an accuracy viewpoint. The enhanced stability by virtue of adopting the upwinding approximation is often overshadowed by the numerically introduced cross-wind diffusion error. This type of error may overspread the solution profile and thus can contaminate the real physics, particularly, for a problem involving a steep gradient of the field variable. As a result, many researchers have attempted to improve the

Received 7 April 2008; accepted 2 April 2009.

The present work was supported by the National Science Council of the Republic of China under Grant NSC97-2628-M-002-022- and CQSE Project 97R0066-69.

Address correspondence to Tony W. H. Sheu, Department of Engineering Science and Ocean Engineering, National Taiwan University, No. 1, Sec. 4, Roosevelt Road, Taipei, Taiwan 10617, Republic of China. E-mail: twhsheu@ntu.edu.tw

NOMENCLATURE

A	amplitude of displacement	L	characteristic length
C_d	drag coefficient $[\equiv F_d / (\frac{1}{2} \rho u^2 d)]$	Re	Reynolds number $(\equiv u_\infty L / \nu)$
C_l	lift coefficient $(\equiv F_l / \frac{1}{2} \rho u^2 d)$	\underline{u}_g	grid velocity vector $[\equiv (u_g, v_g)]$
\underline{f}	body force per unit volume	u_∞	characteristic velocity
\underline{F}_d	drag force	$\underline{\alpha}$	actual wavenumber vector
F_l	lift force	$\underline{\tilde{\alpha}}$	effective wavenumber vector
k	diffusion coefficient defined in Eq. (5)		

prediction accuracy and at the same time to acquire enhanced convective stability. Many ideas have been spawned in the literature to alleviate the problem of accuracy deterioration without sacrificing numerical stability.

Petrov-Galerkin (PG) finite-element methods have been applied with great success to solve the convection-diffusion equation. Among them, the streamline upwind Petrov-Galerkin (SUPG) model of Brooks and Hughes [1] has been most widely applied to predict the flow problem with a prevailing convection. In the presence of boundary and internal sharp layers, the predicted SUPG solution quality can deteriorate further. To resolve the spurious oscillations of these types, Mizukami and Hughes [2] modified the SUPG model and constructed stiffness matrix equations which accommodate the maximum principle [3–5]. Instead of modifying the test functions, Rice and Schnipke [6] and Hill and Baskharone [7] proposed a monotonic finite-element model by integrating the convection term along the local streamline. An exponential weighting function proposed by Ahues and Telies [4] was also shown to be able to construct an M-matrix such that a high-gradient solution can be smoothly captured. The present study is aimed to develop a new bi-quadratic Petrov-Galerkin finite-element model to predict the unsteady incompressible Navier-Stokes (NS) equations at high Reynolds numbers. To enhance the convective stability and retain the dispersive nature, the dispersion relation-preserving (DRP) theory [8] will be adopted in the derivation of the present two-dimensional mixed finite-element model.

In Section 2 the incompressible Navier-Stokes equations are formulated within the arbitrary Lagrangian-Eulerian (ALE) framework. In Section 3 the dispersion relation-preserving theory is applied to solve the convection-diffusion equation so that the dispersion error in the bi-quadratic finite elements can be minimized. In order to verify the proposed dispersion relation-preserving Petrov Galerkin (DRP-PG) finite-element model, in Section 4 several benchmark scalar transport problems and in Section 5 Navier-Stokes problems are investigated. Attention will focus on the scheme effectiveness. In Section 6, the flow fields over an oscillating square and in the contraction-and-expansion channel are analyzed. In Section 7, we conclude this study with some remarks.

2. WORKING EQUATIONS IN MOVING MESH

In a bounded domain, the incompressible Navier-Stokes equations cast in primitive variables \underline{u} and p are considered to investigate the flow motion in viscous

fluids. Subject to the initial and boundary conditions, the dimensionless unsteady elliptic-parabolic partial differential equations can be written as

$$\nabla \cdot \underline{u} = 0 \quad (1)$$

$$\underline{u}_t + \underline{u} \cdot \nabla \underline{u} = -\nabla p + \frac{1}{\text{Re}} \nabla^2 \underline{u} + \underline{f} \quad (2)$$

In Eq. (2), the Reynolds number is defined by $\text{Re} = u_\infty L/\nu$, where ν is the kinematic viscosity of the fluid and L and u_∞ are the user-specified characteristic length and velocity, respectively. Specification of boundary velocities alone is known to be rigorous to close the system of Eqs. (1)–(2) [9]. Any specification of boundary pressure will overdetermine the above elliptic-parabolic time-dependent incompressible NS equations. In this study the continuity and momentum equations (1)–(2) will be solved simultaneously by a mixed finite-element method in order to preserve the mass conservation law unconditionally.

When simulating a time-varying physical problem, the transient incompressible viscous equations need to be solved in the moving meshes. Within the arbitrary Lagrangian-Eulerian framework [10], the geometric conservation law (GCL) [11] is chosen to be the theoretical guidance to calculate the grid velocity \underline{u}_g shown in the following dimensionless working equations, which are formulated in moving meshes [12]:

$$\nabla \cdot \underline{u} = 0 \quad (3)$$

$$\underline{u}_t + (\underline{u} - \underline{u}_g) \cdot \nabla \underline{u} = -\nabla p + \frac{1}{\text{Re}} \nabla^2 \underline{u} + \underline{f} \quad (4)$$

Approximation of grid velocity by means of $\underline{u}_g = (u_g, v_g)[\equiv (x^{\text{new}} - x^{\text{old}})/\Delta t, (y^{\text{new}} - y^{\text{old}})/\Delta t]$ has been shown in [13] to yield the GCL.

3. DISPERSION RELATION-PRESERVING FINITE-ELEMENT MODEL

Due to the resemblance of the linearized incompressible flow equations, the convection-diffusion transport equation with constant diffusion coefficient k and velocity vector $\underline{u} = (u, v)$ given below will be considered in a simply connected domain:

$$\phi_t + u\phi_x + v\phi_y = k(\phi_{xx} + \phi_{yy}) \quad (5)$$

The solution vector for $\hat{\phi}$ is sought by demanding the residual defined by $R = \hat{\phi}_t + u\hat{\phi}_x + v\hat{\phi}_y - k(\hat{\phi}_{xx} + \hat{\phi}_{yy})$ be orthogonal to the space of weighting functions. Within the Petrov-Galerkin context, the test space W_i is chosen to be different from the trial space M_i . By substituting $\hat{\phi} = \sum M_i(\xi, \eta)\phi_i$, where $M_i(i=1, 2, \dots, 9)$ are the bi-quadratic interpolation functions, into the weighted residuals statement, a matrix equation in the nine-node isoparametric bi-quadratic element can be derived.

To develop a computationally stable and numerically accurate weighted-residuals finite-element model, the test space is constructed by adding a rigorously derived stabilizing term along the primary flow direction. The resulting weighting function for Eq. (5) in a domain of mesh size h takes the form $W_i = M_i + \tau h(\partial M_i/\partial x_k)$, where

τ is the undetermined Petrov-Galerkin upwinding coefficient. To eliminate possible spurious pressure modes, the element featured with bi-quadratic basis function M_i for \underline{u} and continuous bi-linear basis function for p is adopted to satisfy the LBB (or the inf-sup) condition. The finite-element approximation of ϕ_x , for example, takes the following form:

$$\begin{aligned}\phi_x &\approx \int_{\Omega} \sum_{j=1}^9 \left(M_j + \tau_j h \frac{\partial M_j}{\partial x} \right) \left(\frac{\partial M_j}{\partial x} \phi_j \right) d\Omega \\ &= \frac{1}{h} \left(\sum_{m=-1, n=-1}^{m=1, n=1} a_k \phi_{i+m, j+n} \right) \quad k = 1, 2, \dots, 9\end{aligned}\quad (6)$$

To develop an advection model accommodating the dispersion relation-preserving property for the first-order derivative terms shown in Eq. (5), it is natural to preserve their numerical dispersion relations. This relation can be derived by conducting the spatial Fourier transform for the first-order derivative term. Thanks to the underlying DRP theory [8], the dispersiveness, dissipation, group and phase velocities for each wave component supported by the first-order derivative term can be well modeled [14]. The modified equation analysis, which involves truncated Taylor series, will be used together with the Fourier transform analysis [15] to get the same or almost the same dispersion relations as ϕ_x and ϕ_y for the advective terms.

The Fourier transform and its inverse for a scalar $\phi(x, y)$ can be respectively expressed by

$$\tilde{\phi}(\alpha, \beta) = \frac{1}{(2\pi)^2} \int_{-\infty}^{+\infty} \int_{-\infty}^{+\infty} \phi(x, y) e^{-i(\alpha x + \beta y)} dx dy \quad (7)$$

$$\phi(x, y) = \int_{-\infty}^{+\infty} \int_{-\infty}^{+\infty} \tilde{\phi}(\alpha, \beta) e^{i(\alpha x + \beta y)} d\alpha d\beta \quad (8)$$

By performing the spatial Fourier transform on each term shown in the algebraic equation for (6), the first component of the actual wavenumber vector $\underline{\alpha} [\equiv (\alpha, \beta)]$ can be derived as

$$\begin{aligned}\alpha &\approx \frac{-i}{h} \left[a_1 e^{-i(\alpha h + \beta h)} + a_2 e^{-i\beta h} + a_3 e^{i(\alpha h - \beta h)} + a_4 e^{-i\alpha h} + a_5 + a_6 e^{i\alpha h} \right. \\ &\quad \left. + a_7 e^{-i(\alpha h - \beta h)} + a_8 e^{i\beta h} + a_9 e^{i(\alpha h + \beta h)} \right]\end{aligned}\quad (9)$$

The right-hand side of Eq. (9), which is regarded as the effective wavenumber $\tilde{\alpha}$ in $\tilde{\underline{\alpha}} = (\tilde{\alpha}, \tilde{\beta})$, is given by

$$\begin{aligned}\tilde{\alpha} &= \frac{-i}{h} \left[a_1 e^{-i(\alpha h + \beta h)} + a_2 e^{-i\beta h} + a_3 e^{i(\alpha h - \beta h)} + a_4 e^{-i\alpha h} + a_5 + a_6 e^{i\alpha h} \right. \\ &\quad \left. + a_7 e^{-i(\alpha h - \beta h)} + a_8 e^{i\beta h} + a_9 e^{i(\alpha h + \beta h)} \right]\end{aligned}\quad (10)$$

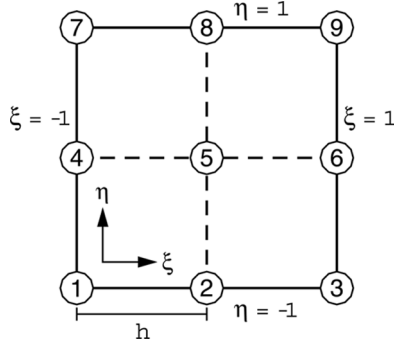


Figure 1. Schematic of a bi-quadratic element. Corner nodes (1, 3, 7, 9), side nodes (2, 4, 6, 8), and center node (5).

where $\mathbf{i} = \sqrt{-1}$. Similarly, the effective wavenumber $\tilde{\beta}$ for ϕ_y can be derived as

$$\tilde{\beta} = \frac{-\mathbf{i}}{h} \left[b_1 e^{-\mathbf{i}(\alpha h + \beta h)} + b_2 e^{-\mathbf{i}\beta h} + b_3 e^{\mathbf{i}(\alpha h - \beta h)} + b_4 e^{-\mathbf{i}\alpha h} + b_5 + b_6 e^{\mathbf{i}\alpha h} + b_7 e^{-\mathbf{i}(\alpha h - \beta h)} + b_8 e^{\mathbf{i}\beta h} + b_9 e^{\mathbf{i}(\alpha h + \beta h)} \right] \quad (11)$$

Note that $\tilde{\alpha}$ approximates α in the sense that it is the wavenumber of the Fourier transform of the PG finite-element equation shown in (6).

To preserve dispersion, the value of $\tilde{\alpha}$ is chosen to make it close to α over an adequate wavenumber range. In the weak sense, the value of $|\alpha h - \tilde{\alpha} h|^2$ (or its integrated error E) should approach zero over a wavenumber range that can adequately define the entire period of the sine (or cosine) wave. For this reason, the wavelengths should be larger than a length that is four times the mesh size h , or $|\alpha h| < \pi/2$. One can therefore define $E(\alpha)$ in the range of $-\pi/2 \leq \gamma_1, \gamma_2 \leq \pi/2$ as follows:

$$E(\alpha) = \int_{-\pi/2}^{\pi/2} \int_{-\pi/2}^{\pi/2} |\alpha h - \tilde{\alpha} h|^2 d(\alpha h) d(\beta h) = \int_{-\pi/2}^{\pi/2} \int_{-\pi/2}^{\pi/2} |\gamma_1 - \tilde{\gamma}_1|^2 d\gamma_1 d\gamma_2 \quad (12)$$

where $(\gamma_1, \gamma_2) = (\alpha h, \beta h)$. To minimize E , the condition given by $\partial E / \partial a_i = 0$, where $i = 1-3, 5, 7-9$, in the schematic in Figure 1, is enforced to derive seven algebraic equations. For the sake of accuracy, Taylor series expansion on $\phi_{i\pm 1, j}$, $\phi_{i, j\pm 1}$, $\phi_{i\pm 1, j\pm 1}$ is performed to eliminate the leading error term shown in the modified equation. By eliminating the coefficient for ϕ and keeping the coefficient as 1 for ϕ_x , two more algebraic equations can be derived. By virtue of the nine theoretically derived algebraic equations, one can calculate the parameters $\tau_1 - \tau_9$, summarized in Table 1, by taking both the accuracy and the dispersion aspects into account. For the detailed expression of τ shown in Eq. (6) using the proposed DRP-PG finite-element model, the reader can refer to [16].

Table 1. Derived DRP-PG parameters for $\tau_1 - \tau_9$

$\tau_7 = -2.240150$	$\tau_8 = 0$	$\tau_9 = 2.240150$
$\tau_4 = 0.560037$	$\tau_5 = 0$	$\tau_6 = -0.560037$
$\tau_1 = -2.240150$	$\tau_2 = 0$	$\tau_3 = 2.240150$

4. VERIFICATION OF THE DRP-PG MODEL

4.1. Convection-Diffusion Problem of Smith and Hutton

The first benchmark problem will be investigated in a square, within which the velocity field is prescribed as $u = 2y(1-x^2)$, $v = -2x(1-y^2)$, as shown in the schematic in Figure 2. Along the line $-1 \leq x \leq 0$, $y = 0$, ϕ is prescribed as [17]

$$\phi(-1 \leq x \leq 0, y = 0) = 1 + \tanh[10(2x + 1)] \quad (13)$$

On the boundaries of $x = -1$, $y = 1$, and $x = 1$, ϕ is specified as $1 - \tanh(10)$. Along the line given by $0 \leq x \leq 1$, $y = 0$, a zero gradient condition for ϕ is imposed.

Given the fixed grid size of $\Delta x = \Delta y = 1/50$, the finite-element solutions will be calculated at $k = 10^{-12}$, 10^{-10} , 10^{-8} , 10^{-6} , 10^{-4} , 10^{-2} , and 10^{-1} . Figures 3a and 3b reveal the efficacy of the proposed finite-element model. The effects of the diffusivity coefficient k and the number of elements are summarized in Figures 3c and 3d based on the simulated solutions plotted at the exit boundary.

4.2. Mixing of Fluids with Different Temperatures

Mixing of warm and cold fluids in a domain of $-4 \leq x, y \leq 4$ is also investigated at $k = 0$. The problem schematic in Figure 4a has the analytical solution $\phi(x, y, t) = -\tanh[(y/2) \cos \omega t - (x/2) \sin \omega t]$ [18], where $\omega (\equiv v_t/v_{\max})$ denotes the rotation frequency and $v_t [\equiv \text{sech}^2(r) \tanh(r)]$ is the tangential velocity at the location which is apart from $(0, 0)$ with a distance of r . The v_{\max} is denoted as the maximum tangential velocity, which is 0.385 for this problem.

The distribution given by $\phi(x, y, t = 0) = -\tanh(y/2)$ will be transported by the specified rotational velocity field ($u = -\omega y$, $v = \omega x$). Figure 4b shows the solution $\phi(x, y, t = 4)$ predicted at $\Delta t = 0.01$ and $\Delta x = \Delta y = 0.1$. Due to the rotating velocity field, the predicted ϕ was seen to take a spiral form, and its value changed sharply near the interface of the warm and cold fluids. The predicted finite-element solutions

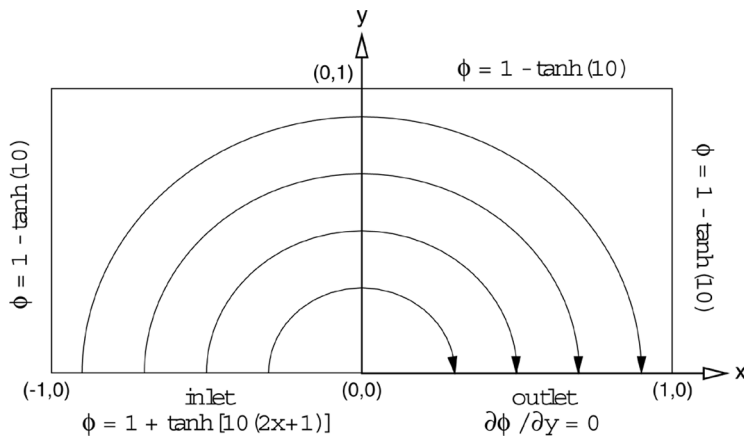


Figure 2. Schematic of the Smith-Hutton problem considered in Section 4.1.

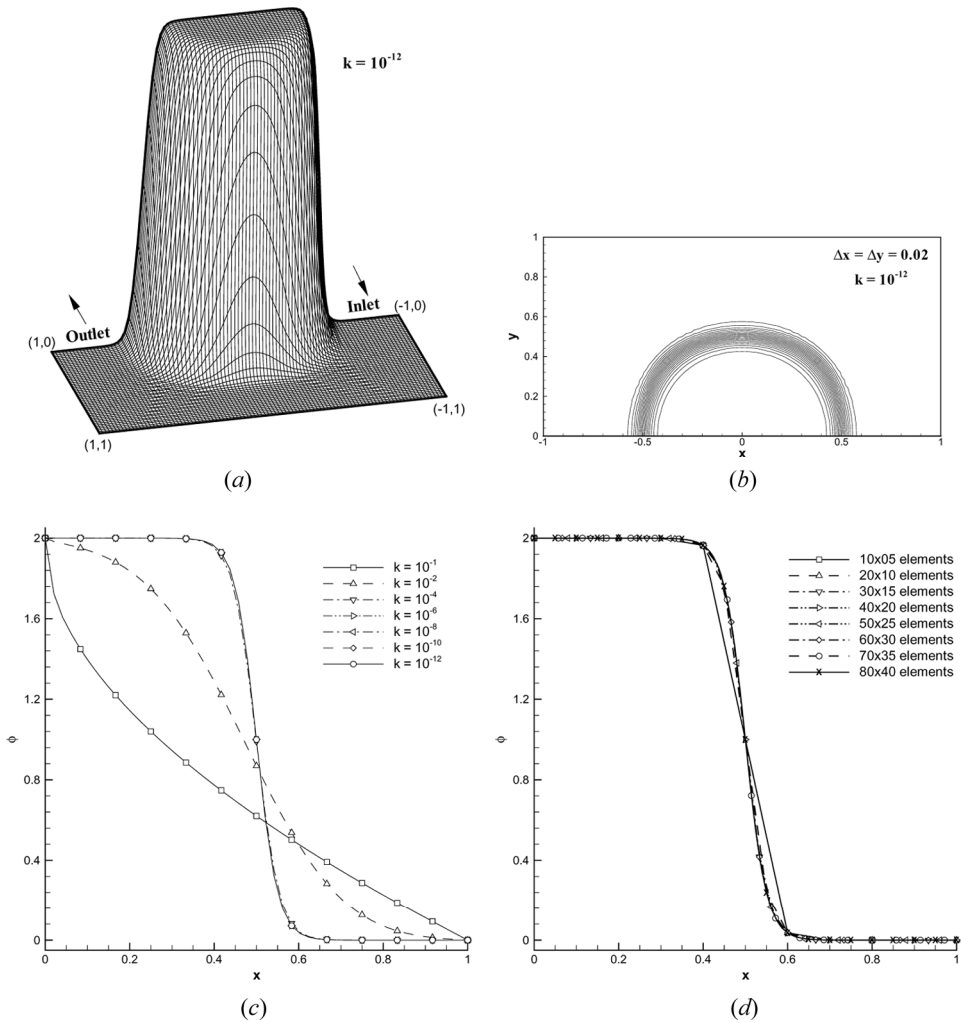


Figure 3. Predicted ϕ solutions at different values of k for the problem considered in Section 4.2 using the proposed DRP-PG finite-element model: (a) solution computed at $k = 10^{-12}$; (b) solution contours computed at $k = 10^{-12}$; (c) solution profiles for $\phi(0 \leq x \leq 1, y = 0)$ obtained at different values of k ; (d) solution profiles for $\phi(0 \leq x \leq 1, y = 0)$ obtained at $k = 10^{-12}$ and different bi-quadratic elements.

plotted in Figure 5 show good agreement with the analytical solutions for the four cases investigated at the angles θ of 0° , 45° , 90° , 135° in the schematic in Figure 4a.

5. VERIFICATION OF THE DRP-PG NAVIER-STOKES MODEL

5.1. Backward-Facing Step Flow Problem

To benchmark the Navier-Stokes finite-element model, the flow in a backward-facing step channel, schematic in Figure 6a, is considered. The expansion

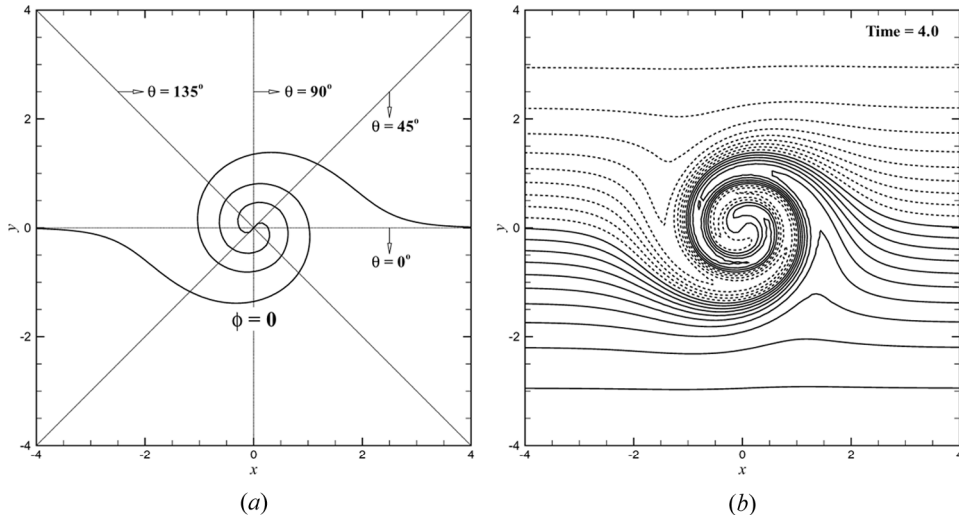


Figure 4. (a) Schematic of the angle θ for the problem considered in Section 4.2, (b) Predicted solution contours.

ratio of the height of the backward-facing step, h , to the height of the downstream channel, H , is $h:H = 1:2$. A fully developed flow profile is prescribed at the inlet. The no-slip condition is imposed at the solid walls, and the traction-free condition [19] is applied at the exit plane. The downstream channel length L is chosen to be $L = 20$ in the current calculation. For the sake of comparison, we define x_1 , as shown in Figure 6a, as the reattachment length of the recirculation region formed downstream of the channel step. We also define x_2 and x_3 as the separation and reattachment lengths of the upper eddy, respectively.

The problem with the boundary conditions schematic in Figure 6b will be investigated at $Re = 100, 200, 400, 600,$ and 800 , where Re is defined on the basis of the downstream channel height H and the average inlet velocity u_{avg} . A parabolic profile $u(0.5 \leq y \leq 1) = 24(1-y)(y-0.5)$ is specified at the channel inlet. A grid spacing of $1/40$ was used for each calculation. The lengths $x_1, x_2,$ and x_3 calculated at different Reynolds numbers are tabulated in Table 2 and plotted in Figure 7a. The solutions obtained at $Re = 800$ show good agreement with the other benchmark results (normalized with H) in Table 3. Also, the benchmark solutions of Gartling [20] for u at $x = 7$ and 15 are plotted in Figure 7b.

5.2. Flow Over a Square Cylinder

The region of current interest is related to the flow over a square cylinder shown in Figure 8, where $x_u = 5, d = 1, x_d = 20,$ and $H = 13$. The height of the square cylinder (d) and the average velocity at the inflow boundary (u) are used to normalize the length and the velocity, respectively. The boundary conditions involve prescribing the uniform inflow velocity ($u = 1, v = 0$), the no-slip condition ($u = v = 0$) on the square surface, $\partial u / \partial y = v = 0$ at the upper and lower boundaries, and the traction-free condition on the outlet boundary.

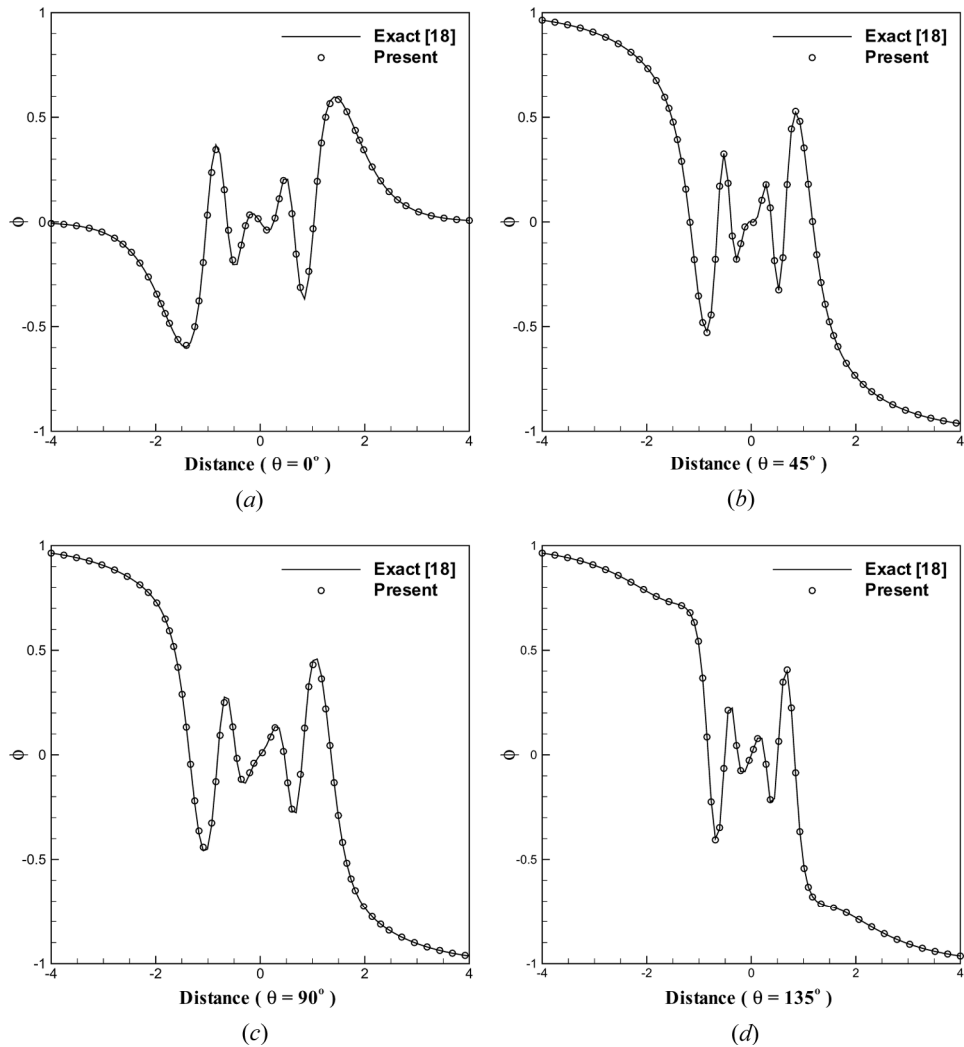


Figure 5. Comparison of analytic and predicted solutions for the problem considered in Section 4.2. The angle θ was defined in Figure 4a. (a) $\theta = 0^\circ$; (b) $\theta = 45^\circ$; (c) $\theta = 90^\circ$; (d) $\theta = 135^\circ$.

The forces acting on the square cylinder can be subdivided into the drag coefficient (C_d) and the lift coefficient (C_l), which are defined respectively as $F_d/(\frac{1}{2}\rho u^2 d)$ and $F_l/(\frac{1}{2}\rho u^2 d)$, where F_d and F_l are known as the drag and lift forces induced on the square cylinder. These two forces are obtained by appropriately integrating the pressure and shear-stress resistances over the square prism. The lift force fluctuation is directly associated with the eddy formation and eddy shedding, and therefore its magnitude will be varied between a positive and a negative maximum.

The time histories of C_d , C_l , and other integral parameters show a periodic structure with a dominant harmonic at different Reynolds numbers. Each cycle involves a pair of shedding eddies from the prism. The drag coefficient is oscillated at twice the

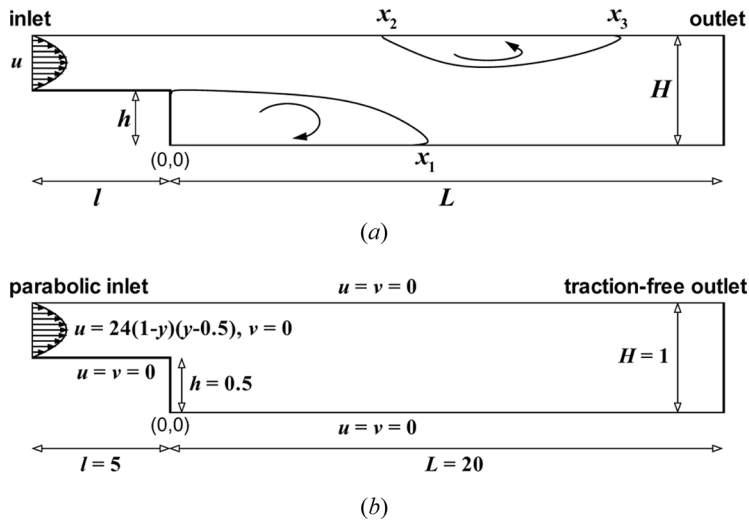


Figure 6. Schematic of backward-facing step problem considered in Section 5.1: (a) geometry and illustration of two recirculation regions; (b) boundary conditions.

frequency of the lift coefficient, as the drag is not sensitive to the asymmetry of the shedding. Table 4 summarizes some useful design parameters obtained at different Reynolds numbers, such as the time-averaged drag coefficient ($\overline{C_d}$), the root-mean-square lift coefficient ($C_{l,rms}$), and the Strouhal number (S_t). Here, $C_{l,rms}$ is defined as $(\overline{C_l^2})^{1/2}$, while the Strouhal number S_t is given by fd/u , where the vortex shedding frequencies f (shown in Figure 9) are calculated from the power-spectrum analysis. The present results show good agreement with the benchmark data given in Tables 5 and 6.

6. NUMERICAL RESULTS

6.1. Flow Over a Square Cylinder Oscillating along the x Direction

Fluid flow over a square cylinder (prism), which is oscillated along the mean flow direction, will be investigated at $Re = 200$. The purpose of performing this simulation is to study the interaction between the vortex-shedding and the forced cylinder oscillations. Also, the occurrence of lock-in phenomenon and the influence of

Table 2. Predicted reattachment and separation lengths (schematic in Figure 6a), versus Reynolds numbers

	Re				
	100	200	400	600	800
x_1	1.4484	2.4967	4.1900	5.2032	5.7396
x_2	—	—	—	4.3688	4.6500
x_3	—	—	—	7.8390	10.0211

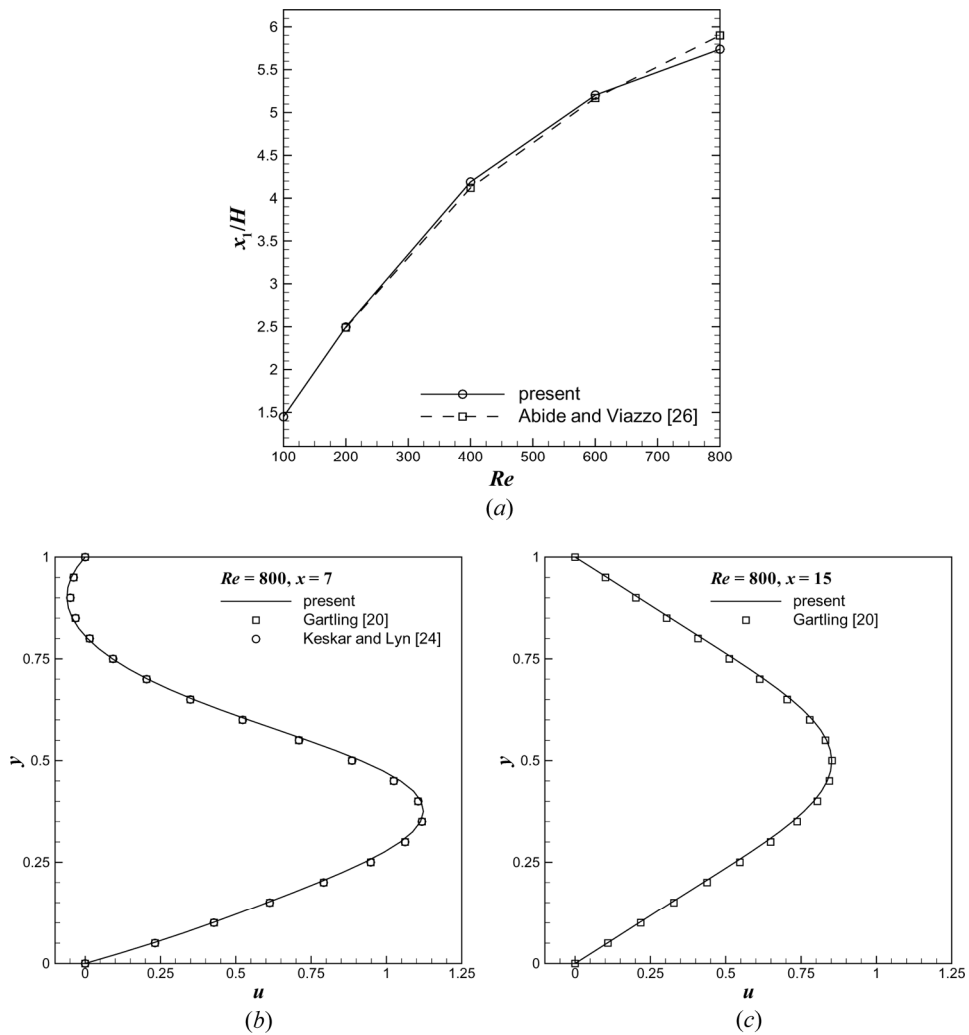


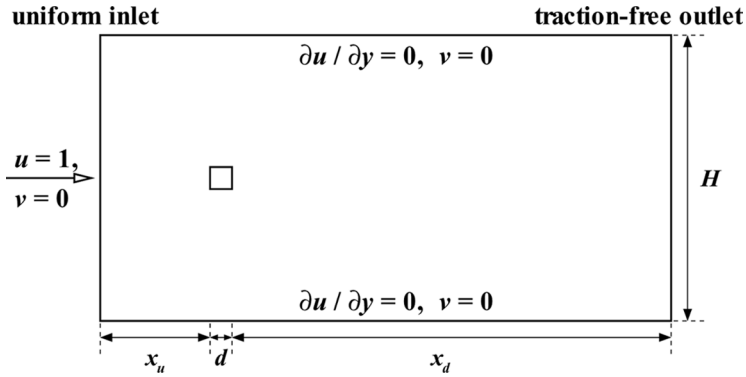
Figure 7. Comparison of predicted solution with other predicted results: (a) reattachment lengths x_1 ; (b) u -velocity profiles at $x=7$; (c) u -velocity profiles at $x=15$.

frequency and amplitude on the cylinder oscillations will be investigated. For the sake of accuracy, a very fine grid is distributed near the edges of the cylinder because of the large velocity and pressure gradients in this region. The dimensionless time step $\Delta t=0.05$ was selected for the case considered at $Re=200$.

A square cylinder is forced to oscillate harmonically along the uniform flow as shown in Figure 10. The displacement of the cylinder is given by $x=A\sin(2\pi f_c t)$, where A is the oscillation amplitude and f_c is the cylinder oscillating frequency. The boundary conditions are similar to those of the stationary case considered in the previous section. The fixed cylinder corresponds to the case considered at $A=0$, and it is the reference case for the evaluation of numerical results, which will

Table 3. Comparison of dimensionless reattachment and separation lengths (schematic in Figure 6a), for backward-facing step flow problem investigated at $Re = 800$

Authors		Lower eddy reattachment x_1/H	Upper eddy separation x_2/H	Upper eddy reattachment x_3/H
Without inlet channel	Gartling [20]	6.10	4.85	10.48
	Gresho et al. [21] (FDM)	6.08	4.84	10.46
	Gresho et al. [21] (SEM)	6.10	4.86	10.49
	Sani and Gresho [22]	6.22	5.09	10.25
	Barton [23]	6.02	4.82	10.48
	Keskar and Lyn [24]	6.10	4.85	10.48
With inlet channel	Barton [23]	5.75	4.57	10.33
	Wan et al. [25]	5.02	—	—
	Abide and Viazzo [26]	5.90	—	—
	Present	5.64	4.65	10.02

**Figure 8.** Schematic of computational domain and boundary conditions for flow over a square cylinder considered in Section 5.2.**Table 4.** Predicted parameters at different Reynolds numbers for flow over a square cylinder

Re	$\overline{C_d}$	$\overline{C_{dp}}$	$C_{l,rms}$	S_t	Δt
45	1.764	1.522	—	—	0.05
50	1.696	1.487	—	—	0.05
55	1.669	1.481	0.051	0.124	0.05
100	1.481	1.425	0.134	0.142	0.05
200	1.449	1.481	0.316	0.164	0.05

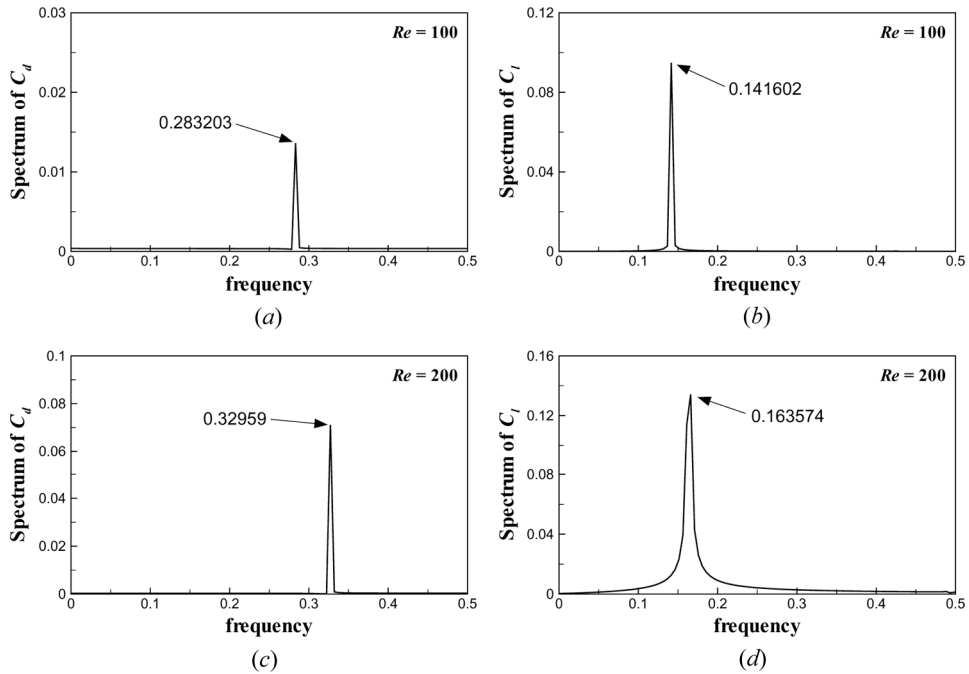


Figure 9. Predicted power spectrum for drag and lift coefficients at $Re = 100$ and 200: (a) drag coefficient at $Re = 100$; (b) lift coefficient at $Re = 100$; (c) drag coefficient at $Re = 200$; (d) lift coefficient at $Re = 200$.

be presented later. We also define f_o as the natural shedding frequency and f_v as the vortex-shedding frequency. The simulated natural shedding frequency $f_o = 0.164$ shows good agreement with the reference values given in Table 6 at $Re = 200$.

A closer inspection of the flow reveals that the square motion can control the instability mechanism that will result in a vortex shedding. Hence, the flow generated by such a vortex shedding around a vibrating bluff body can cause a significant difference from the flow around a fixed cylinder to occur. When the cylinder is forced to oscillate, two periodic motions, one with the vortex-shedding frequency f_o and the

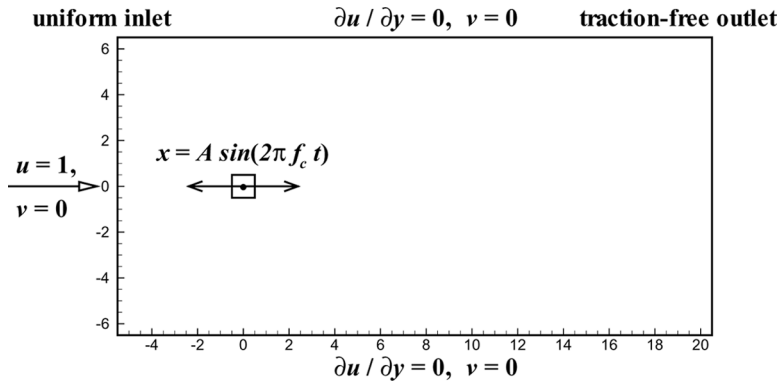
Table 5. Comparison of predicted $\overline{C_d}$, $C_{l,rms}$, and S_l for flow over a square cylinder at $Re = 100$

Authors	$\overline{C_d}$	$C_{l,rms}$	S_l
Okajima [27]	—	—	0.135
Davis and Moore [28]	1.640	—	0.153
Franke et al. [29]	1.610	—	0.154
Arnal et al. [30]	1.420	—	0.153
Li and Humphrey [31]	1.750	—	0.141
Sohankar et al. [32]	1.478	0.153	0.146
Pavlov et al. [33]	1.510	0.137	0.150
Wan et al. [25]	1.523	0.148	0.153
Present	1.481	0.134	0.142

Table 6. Comparison of predicted $\overline{C_d}$, $C_{l,rms}$, and S_l for flow over a square cylinder at $Re = 200$

Authors	$\overline{C_d}$	$C_{l,rms}$	S_l
Okajima [27]	—	—	0.140
Davis and Moore [28]	1.710	—	0.165
Franke et al. [29]	1.600	—	0.157
Steggel and Rockliff [34]	1.466	0.353	0.154
Sohankar et al. [32]	1.462	0.377	0.150
Pavlov et al. [33]	1.560	0.376	0.156
Present	1.449	0.316	0.164

other with the forced cylinder motion frequency f_c , will interact with each other. This interaction is responsible for the flow phenomena which are manifested by the ratio f_c/f_o and the dimensionless maximum cylinder displacement A . These parameters can be used to characterize various interference regimes. The relationship of f_o , f_c , and f_v shown in Figure 11 confirms the presence of the lock-in phenomenon that was previously predicted by Steggel and Rockliff [34]. A flow regime with a strong interaction, called the lock-in phenomenon, between the forced cylinder motion and the natural vortex shedding describes the synchronization of the two oscillations. The natural vortex shedding adapts its frequency to that of the forced cylinder motion. The occurrence of the lock-in phenomenon depends on the frequency (f_c) and the amplitude (A) of the forced cylinder motion. Each data point plotted in Figure 11 is the result of a separate calculation, and the discrete points have been connected by a line for better illustration of the plateau predicted in the vicinity of $f_c/f_o = 2$, at which the lock-in phenomenon occurs. This graphical evaluation is proper for demonstrating the interaction between frequencies f_c and f_v . When there is no interaction, the vortex-shedding frequency f_v and the natural frequency f_o observed over the fixed cylinder are of equal magnitude. The value of f_c at which the lock-in phenomenon occurs depends on the amplitude A .

**Figure 10.** Schematic of flow over a square cylinder, oscillating along the x direction, considered in Section 6.1.

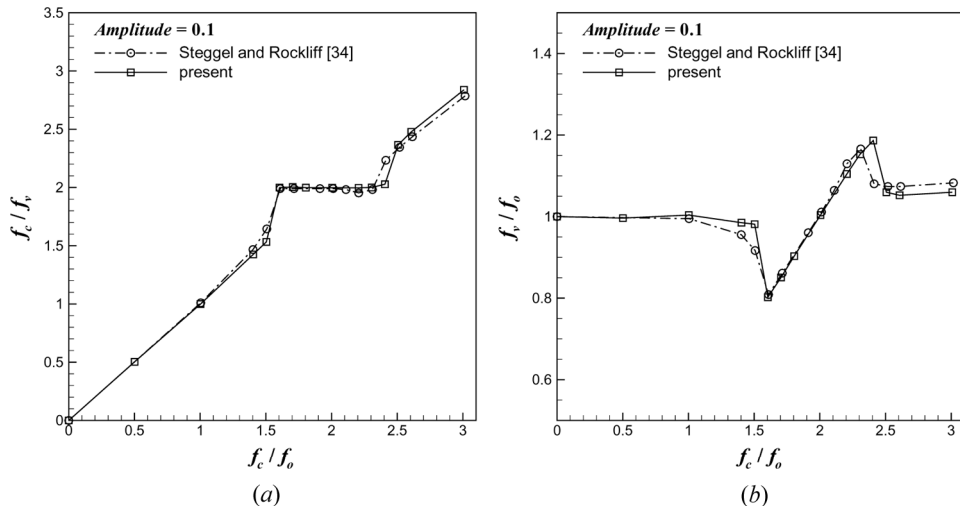


Figure 11. Determination of frequency range in which lock-in occurs, by plotting f_c/f_v and f_v/f_o against f_c/f_o at $Re = 200$: (a) f_c/f_v versus f_c/f_o ; (b) f_v/f_o versus f_c/f_o .

6.2. Flow in a Time-Varying Contraction-and-Expansion Channel

In the two-dimensional contraction-and-expansion channel schematic in Figure 12a, the height of the contraction and expansion are represented as h and H , respectively. The Reynolds number is defined by $Re = uh/\nu$, where u is the average u velocity in the contraction channel and ν is the kinematic viscosity of the working fluid. All the results were calculated in nonuniform grids, as shown in Figure 12b,

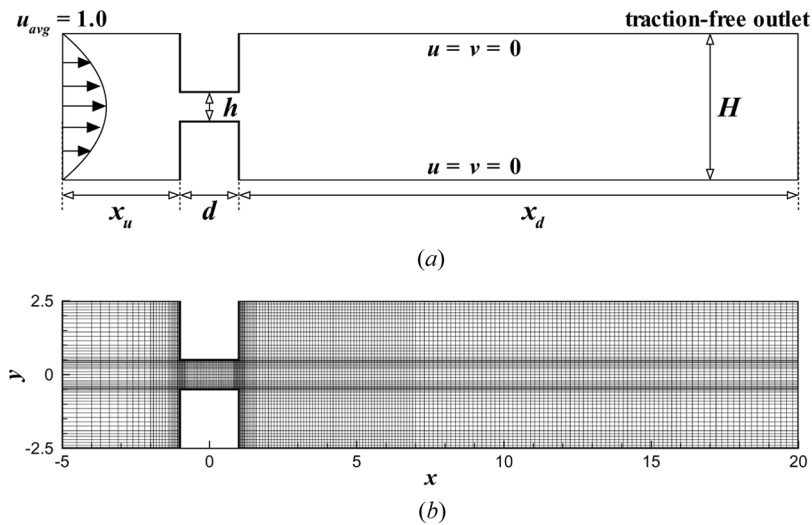


Figure 12. Illustration of contraction-and-expansion problem considered in Section 6.2: (a) computational domain and boundary conditions; (b) mesh system.

at the dimensionless geometric parameters $x_u=4$, $d=2$, $x_d=100$, $h=1$, and $H=5$. Since there are no proper data for comparison, the simulated u -velocity profiles are compared with the results obtained from the CFD-ACE+ commercial software [35]. The compared results in Figure 13 show very good agreement.

It has been observed that the flow pattern is symmetrical about the centerline of the channel at the Reynolds number below its critical value. There exists only a single stable flow pattern in which the regions of recirculating flow, which occurs in the vicinity of the channel walls immediately downstream of the expansion, have the same size at the two channel sides. The critical Reynolds number, above which the flow behavior becomes substantially different from that observed below this value, depends on the channel geometry, which is characterized by the dimensionless expansion ratio E . This ratio is defined as the ratio of the channel height at the downstream end of the expansion, H , to the upstream channel height of the contraction, h . Here, we consider $E=H/h=5$ for all the calculations.

The regions of recirculation became large, extending farther downstream of the expansion location, as the Reynolds number is increased. The predicted results show that the solutions obtained at $Re=50$, 100 , and 200 are asymmetric, with the detached flow being directed toward one or the other channel wall. In these cases, one of the two recirculation regions appearing immediately downstream of the expansion becomes larger at the expense of the other. When the flow pattern becomes no longer symmetric, a process known as the bifurcation is said to occur.

The contraction part of the contraction-and-expansion channel is then forced to oscillate. The schematic of the vibration is shown in Figure 14. The displacement of the contraction channel h is given by $h=A\sin(2\pi f_c t)$, where A is the oscillation

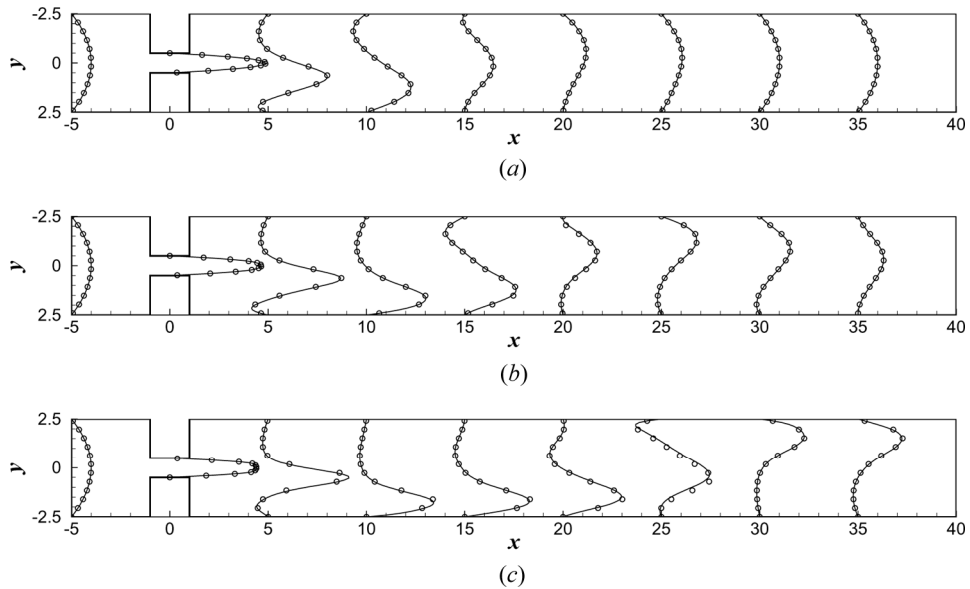


Figure 13. Comparison of predicted u -velocity profiles (circles \circ) and CFD-ACE+ results (solid curves) for the purpose of comparison: (a) $Re=50$; (b) $Re=100$; (c) $Re=200$.

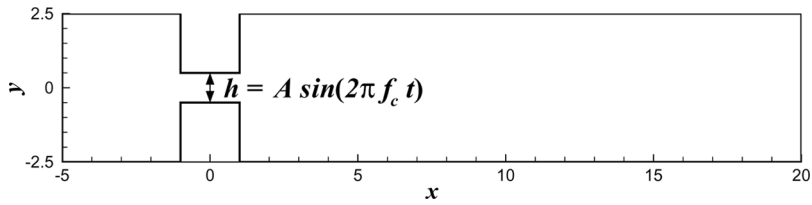


Figure 14. Schematic of the oscillatory contraction section.

amplitude and f_c is the vibration frequency. Here, the case, featured with $A = 0.2$ and $f_c = 100$, investigated at $Re = 100$, will be considered. With the oscillation of the contraction part, the flow field shown in Figure 15a becomes turbulent and gradually transits into a periodic steady state. The power spectrum of the periodic steady state C_l shown in Figure 15b shows that the frequency of the flow field is equal to the frequency of the oscillating duct. This implies that the nonlinear behavior is not strong enough and the bifurcation phenomenon in the flow field is dominated by the forced oscillation. The predicted streamline contours over one complete oscillation period are plotted in Figure 16, from which it is observed that the downstream flow is asymmetric and complex.

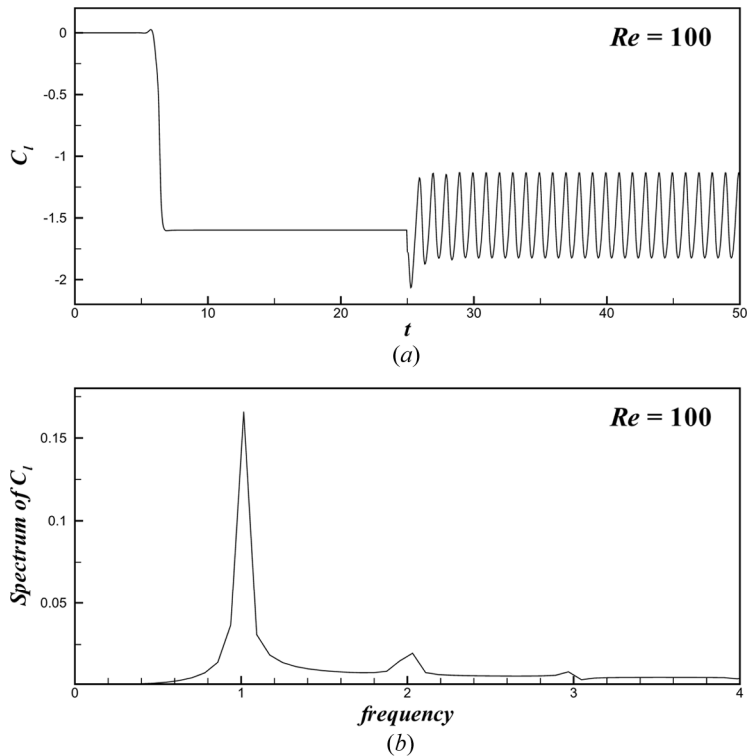


Figure 15. Predicted time-evolving solutions for the case considered at $Re = 100$: (a) lift coefficient; (b) power spectrum.

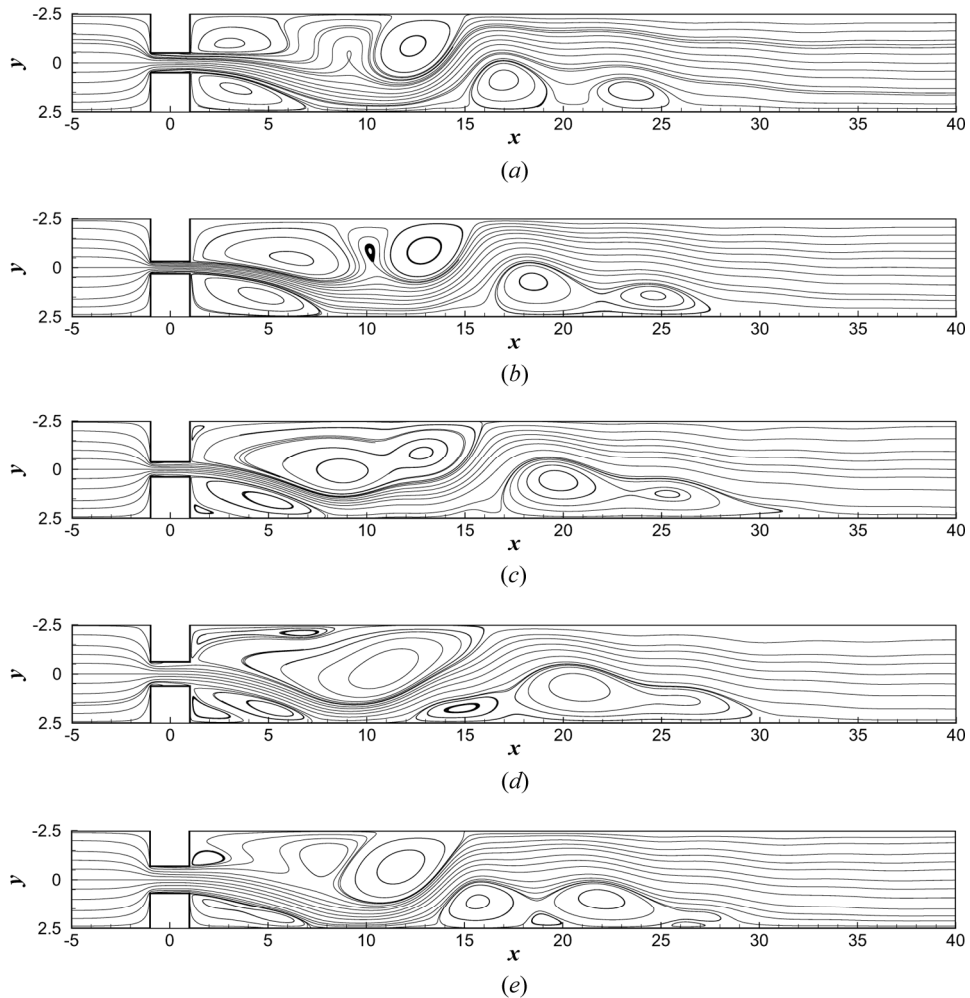


Figure 16. Predicted streamline contours over a complete contraction oscillation period ($T = 1/f_c$) for the case considered at $Re = 100$, $A = 0.2$, and $f_c = 100$: (a) $t = T/10$; (b) $t = 3T/10$; (c) $t = 5T/10$; (d) $t = 7T/10$; (e) $t = 9T/10$.

7. CONCLUDING REMARKS

The present study developed a bi-quadratic Petrov-Galerkin finite-element model for solving the unsteady convection-diffusion transport equation and the incompressible Navier-Stokes equations in both stationary and moving meshes. To enhance the convective stability and retain the dispersive nature, the dispersion relation-preserving theory was employed to develop a two-dimensional mixed finite-element model. Two scalar problems amenable to exact solutions were investigated for the sake of verification. The simulated results were shown to be in perfect agreement with the exact solutions, thus demonstrating the integrity of the present method. The Navier-Stokes fluid flows in a backward-facing step channel and over

a square cylinder were also investigated at different Reynolds numbers. The predicted DRP-PG finite-element solutions agreed perfectly with the benchmark solutions. The incompressible flow problem with a moving boundary was analyzed within the arbitrary Lagrangian-Eulerian framework. The problem for the flow over an oscillating square cylinder was chosen for verification purposes. From the simulated results, it was observed that the present method is highly reliable and can be applicable to study moving-boundary problems numerically. The method was also applied to understand the internal flow in a partially oscillating channel. From the predicted results, it was noticed that the flow field downstream of the contraction-and-expansion part was asymmetric and complex.

REFERENCES

1. A. N. Brooks and T. J. R. Hughes, Streamline Upwind/Petrov-Galerkin Formulations for Convection Dominated Flows with Particular Emphasis on the Incompressible Navier-Stokes Equations, *Comput. Meth. Appl. Mech. Eng.*, vol. 32, pp. 199–259, 1982.
2. A. Mizukami and T. J. R. Hughes, A Petrov-Galerkin Finite-Element Method for Convection Dominated Flow: An Accurate Upwinding Technique for Satisfying the Maximum Principle, *Comput. Meth. Appl. Mech. Eng.*, vol. 50, pp. 181–193, 1985.
3. T. Meis and U. Marcowitz, *Numerical Solution of Partial Differential Equations*, Lecture Notes in Applied Mathematical Science, vol. 32, Springer-Verlag, New York, 1981.
4. M. Ahues and M. Telias, Petrov-Galerkin Schemes for the Steady State Convection-Diffusion Equation, in K. P. Holz (ed.), *Finite Elements in Water Resources: Proceedings of the 4th International Conference*, Springer-Verlag, Berlin, 1982.
5. T. Ikeda, *Maximal Principle in Finite Element Models for Convection-Diffusion Phenomena*, Lecture Notes in Numerical and Applied Analysis, vol. 4, North-Holland, Amsterdam, 1983.
6. J. G. Rice and R. J. Schnipke, A Monotone Streamline Upwind Finite Element Method for Convection-Diffusion Flows, *Comput. Meth. Appl. Mech. Eng.*, vol. 47, pp. 313–327, 1984.
7. D. L. Hill and E. A. Baskharone, A Monotone Streamline Upwind Method for Quadratic Finite Elements, *Int. J. Numer. Meth. Fluids*, vol. 17, pp. 463–475, 1993.
8. C. K. W. Tam and J. C. Webb, Dispersion-Relation-Preserving Finite Difference Schemes for Computational Acoustics, *J. Comput. Phys.*, vol. 107, pp. 262–281, 1993.
9. O. Ladyzhenskaya, *The Mathematical Theory of Viscous Incompressible Flow*, Gordon & Breach, New York, 1969.
10. J. Donea, An Arbitrary Lagrangian-Eulerian Finite Element Method for Transient Fluid-Structure Interactions, *Comput. Meth. Appl. Mech. Eng.*, vol. 33, pp. 689–723, 1982.
11. P. D. Thomas and C. K. Lombard, Geometric Conservation Law and Its Application to Flow Computations on Moving Grids, *AIAA J.*, vol. 17, pp. 1030–1037, 1979.
12. T. W. H. Sheu and Y. H. Chen, A Transient Analysis of Flow in Vessels with Moving Boundaries, *Int. J. Numer. Meth. Heat Fluid Flow*, vol. 9, pp. 833–846, 1999.
13. Y. H. Chen and T. W. H. Sheu, Finite-Element Simulation of Incompressible Fluid Flow in an Elastic Vessel, *Int. J. Numer. Meth. Fluids*, vol. 42, pp. 131–146, 2003.
14. F. Q. Hu, M. Y. Hussaini, and J. L. Manthey, Low-Dissipation and Low-Dispersion Runge-Kutta Schemes for Computational Acoustics, *J. Comput. Phys.*, vol. 124, pp. 177–191, 1996.
15. R. K. Lin and T. W. H. Sheu, Application of Dispersion-Relation-Preserving Theory to Develop a Two-Dimensional Convection-Diffusion Scheme, *J. Comput. Phys.*, vol. 208, pp. 493–526, 2005.

16. M. C. Hsu, On a Two-Dimensional Dispersively Accurate Petrov-Galerkin Model for Incompressible Navier-Stokes Equations on Moving Meshes, master's thesis, Department of Engineering Science and Ocean Engineering, National Taiwan University, Taipei, Taiwan, 2005.
17. R. M. Smith and A. G. Hutton, The Numerical Treatment of Advection: A Performance Comparison of Current Methods, *Numer. Heat Transfer B*, vol. 5, pp. 439–461, 1982.
18. P. Tamamidis and D. N. Assanis, Evaluation for Various High-Order-Accuracy Schemes with and without Flux Limiters, *Int. J. Numer. Meth. Fluids*, vol. 16, pp. 931–948, 1993.
19. M. T. Wang and T. W. H. Sheu, Implementation of a Free Boundary Condition to Navier-Stokes Equations, *Int. J. Numer. Meth. Fluids*, vol. 7, pp. 95–111, 1997.
20. D. K. Gartling, A Test Problem for Outflow Boundary Conditions—Flow over a Backward-Facing Step, *Int. J. Numer. Meth. Fluids*, vol. 11, pp. 953–967, 1990.
21. P. M. Gresho, D. K. Gartling, K. H. Winters, T. J. Garratt, A. Spence, and J. W. Goodrich, Is the Steady Viscous Incompressible Two-Dimensional Flow over a Backward-Facing Step at $Re=800$ Stable? *Int. J. Numer. Meth. Fluids*, vol. 17, pp. 501–541, 1993.
22. R. L. Sani and P. M. Gresho, Résumé and Remarks on the Open Boundary Condition Minisymposium, *Int. J. Numer. Meth. Fluids*, vol. 18, pp. 983–1008, 1994.
23. I. E. Barton, The Entrance Effect of Laminar Flow over a Backward-Facing Step Geometry, *Int. J. Numer. Meth. Fluids*, vol. 25, pp. 633–644, 1997.
24. J. Keskar and D. A. Lyn, Computations of a Laminar Backward-Facing Step Flow at $Re=800$ with a Spectral Domain Decomposition Method, *Int. J. Numer. Meth. Fluids*, vol. 29, pp. 411–427, 1999.
25. D. C. Wan, B. S. V. Patnail, and G. W. Wei, Discrete Singular Convolution-Finite Subdomain Method for the Solution of Incompressible Viscous Flows, *J. Comput. Phys.*, vol. 180, pp. 229–255, 2002.
26. S. Abide and S. Viazzo, A 2D Compact Fourth-Order Projection Decomposition Method, *J. Comput. Phys.*, vol. 206, pp. 252–276, 2005.
27. A. Okajima, Strouhal Numbers of Rectangular Cylinders, *J. Fluid Mech.*, vol. 123, pp. 379–398, 1982.
28. R. W. Davis and E. F. Moore, A Numerical Study of Vortex Shedding from Rectangles, *J. Fluid Mech.*, vol. 116, pp. 475–506, 1982.
29. R. Franke, W. Rodi, and B. Schöning, Numerical Calculation of Laminar Vortex-Shedding Flow Past Cylinders, *J. Wind Eng. Ind. Aerodyn.*, vol. 35, pp. 237–257, 1990.
30. M. P. Arnal, D. J. Goering, and J. A. C. Humphrey, Vortex Shedding from a Bluff Body Adjacent to a Plane Sliding Wall, *J. Fluids Eng.*, vol. 113, pp. 384–398, 1991.
31. G. Li and J. A. C. Humphrey, Numerical Modelling of Confined Flow past a Cylinder of Square Cross-Section at Various Orientations, *Int. J. Numer. Meth. Fluids*, vol. 20, pp. 1215–1236, 1995.
32. A. Sohankar, C. Nurberg, and L. Davidson, Low-Reynolds-Number Flow around a Square Cylinder at Incidence: Study of Blockage, Onset of Vortex Shedding and Outlet Boundary Condition, *Int. J. Numer. Meth. Fluids*, vol. 26, pp. 39–56, 1998.
33. A. N. Pavlov, S. S. Sazhin, R. P. Fedorenko, and M. R. Heikal, A Conservative Finite Difference Method and Its Application for the Analysis of a Transient Flow around a Square Prism, *Int. J. Numer. Meth. Heat & Fluids Flow*, vol. 10, pp. 6–46, 2000.
34. N. Steggel and N. Rockliff, Simulation of the Effects of Body Shape on Lock-in Characteristics in Pulsating Flow by the Discrete Vortex Method, *J. Wind Eng. Ind. Aerodyn.*, vol. 69–71, pp. 317–329, 1997.
35. CFD Research Corporation (CFDRC), *CFD Research Corp. (CFDRC) Engineering Simulations Software, Services and R&D*, www.cfdrc.com, 2005.